Science Advances

Supplementary Materials for

Nonvolatile infrared memory in MoS$_2$/PbS van der Waals heterostructures

Qisheng Wang, Yao Wen, Kaiming Cai, Ruiqing Cheng, Lei Yin, Yu Zhang, Jie Li, Zhenxing Wang, Feng Wang, Fengmei Wang, Tofik Ahmed Shifa, Chao Jiang, Hyunsoo Yang, Jun He

This PDF file includes:

- fig. S1. Chemical and structural characterization.
- fig. S2. Device morphology and optoelectronic transport.
- fig. S3. Control experiments on few-layer MoS$_2$.
- fig. S4. Photoresponse in PbS nanoplate with an 808-nm laser illumination.
- fig. S5. The optoelectronic transport and optical memory.
- fig. S6. Photoresponse performance.
- fig. S7. V_g pulse–dependent erasing current.
- fig. S8. Optoelectronic transport and on/off ratio.
- fig. S9. Persistent photocurrent as a function of time after the laser pulse switches off.
- fig. S10. Optoelectronic transport and optical memory.
- fig. S11. Number of transferred electrons as a function of the Fermi level shift.
- table S1. Memory performance of five devices.
- note S1. Theoretical simulation of carrier injection to MoS$_2$.
- note S2. Dynamics analysis of V_g pulse erasing.
- note S3. Roles of disorder states on the optical memory.
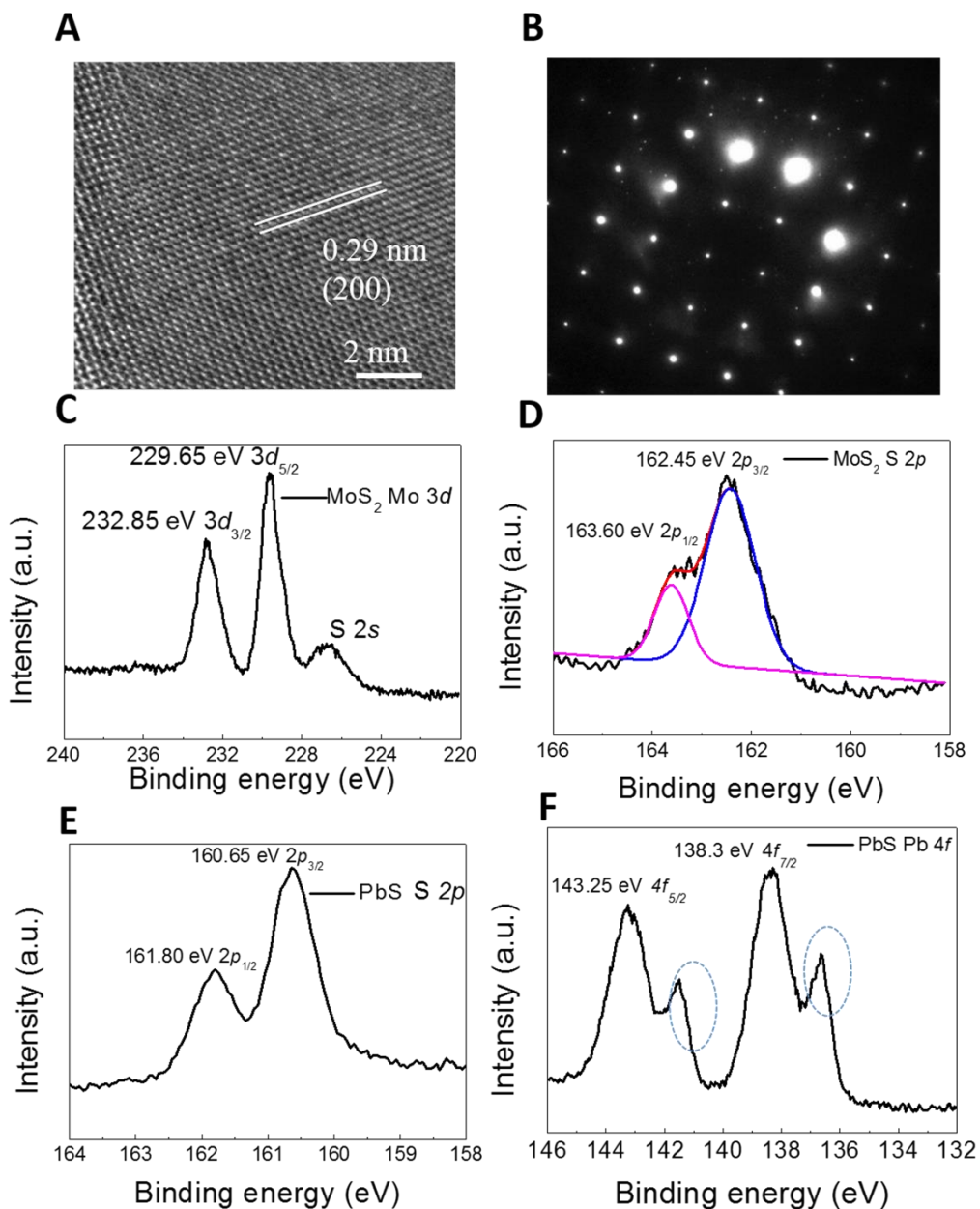- note S4. Photothermal effect or Schottky barrier effect.
- References (*36–43*)

fig. S1. **Chemical and structural characterization.** (**A**) HRTEM and (**B**) SAED pattern of PbS nanoplate. XPS for (**C**) Mo $3d$ and (**D**) S $2p$ from few-layer MoS_2 in heterostructure. (**E**) and (**F**) are XPS for S $2p$ and Pb $4f$ from PbS nanoplates respectively. The dashed blue circles in (**F**) point out two additional peaks from XPS spectra of Pb $4f$, which origin from pure Pb metal mixed with PbS nanoplates.
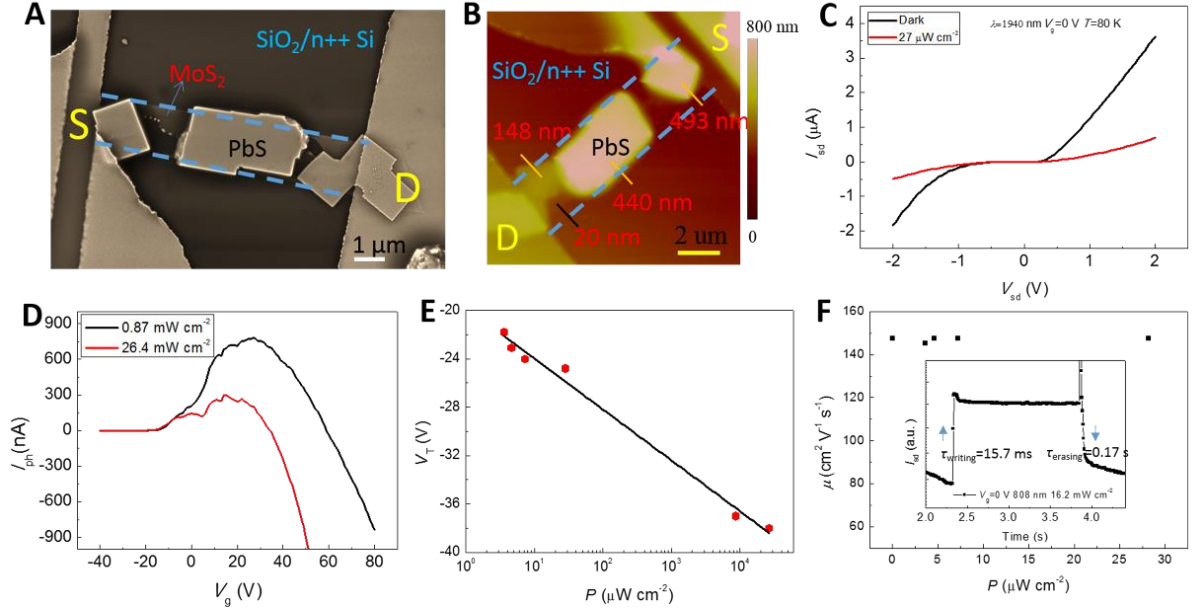
fig. S2. **Device morphology and optoelectronic transport.** (**A**) SEM and (**B**) AFM images of device #1. The few-layer MoS_2 was connected to Ti (10 nm)/Au (40 nm) electrodes. The thickness of few-layer MoS_2 is 20 nm. The channel length L=9.33 μm and width W=1.64 μm. (**C**) The I_{sd}-V_{sd} curves under illumination of 1940 nm laser. The device shows a negative photoresponse at $V_g = 0$ V, which is consistent with the photoresponse of 808 nm illumination at a low power density. (**D**) Photocurrent I_{ph} versus back gate voltage V_g under illumination of 808 nm laser with a high power density ($P \geq 0.87$ mW cm^{-2}). (**E**) P-dependent threshold voltage V_T of transfer characteristic curves shown in Fig. 1(C). (**F**) Field effect mobility μ of few-layer MoS_2 in heterostructure extracted from Fig. 1C with $P \leq 28.2$ μW cm^{-2}. The field effect mobility was estimated based on the gate capacitance effect (*36*) $\mu = \dfrac{L}{WC_iV_{sd}}(\dfrac{dI_{sd}}{dV_g})$,

where $\dfrac{dI_{sd}}{dV_g}$ is given by the maximum slope of transfer characteristic curves, $C_i = 1.23 \times 10^{-4} F/m^2$ is the capacitance of the SiO$_2$ dielectric layer. Inset of (F) is one cycle showing the writing and erasing time. The P is 16.2 mW cm^{-2}.
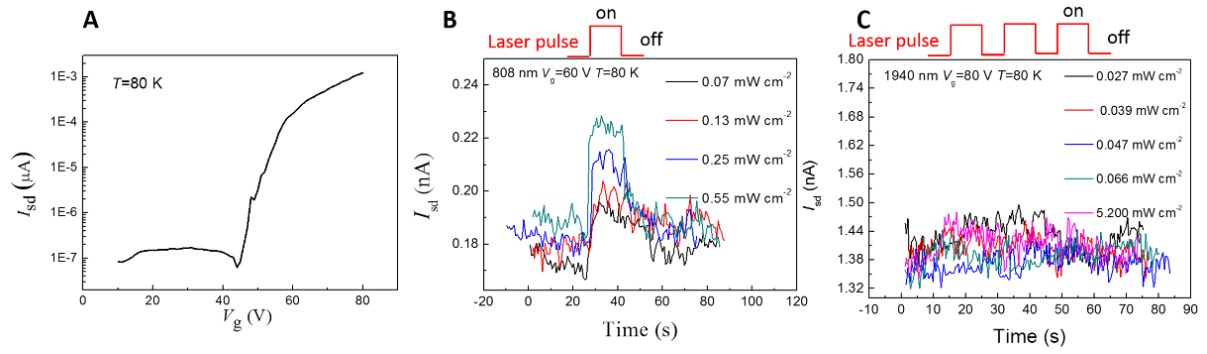
fig S3. **Control experiments on few-layer MoS₂.** (**A**) Transfer characteristic curve (I_{sd} versus V_g) of few-layer MoS$_2$ at 80 K. (**B** and **C**) Time evolution of I_{sd} under illumination of 808 and 1940 nm laser pulse, respectively. The pulse width is 10 s. V_{sd} equals to 2 V.
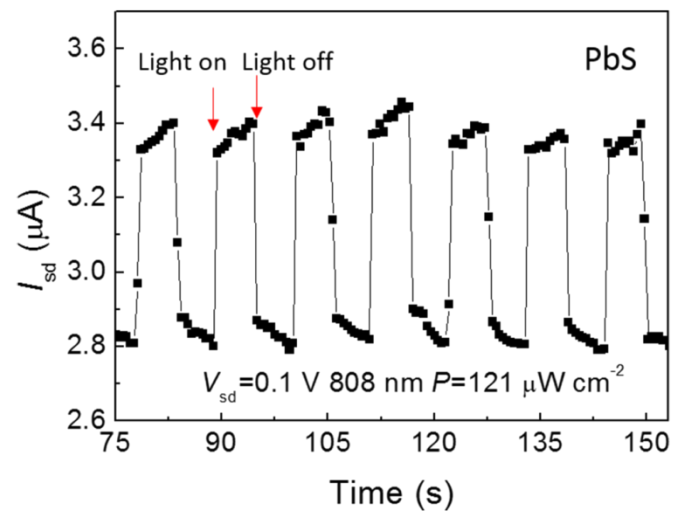

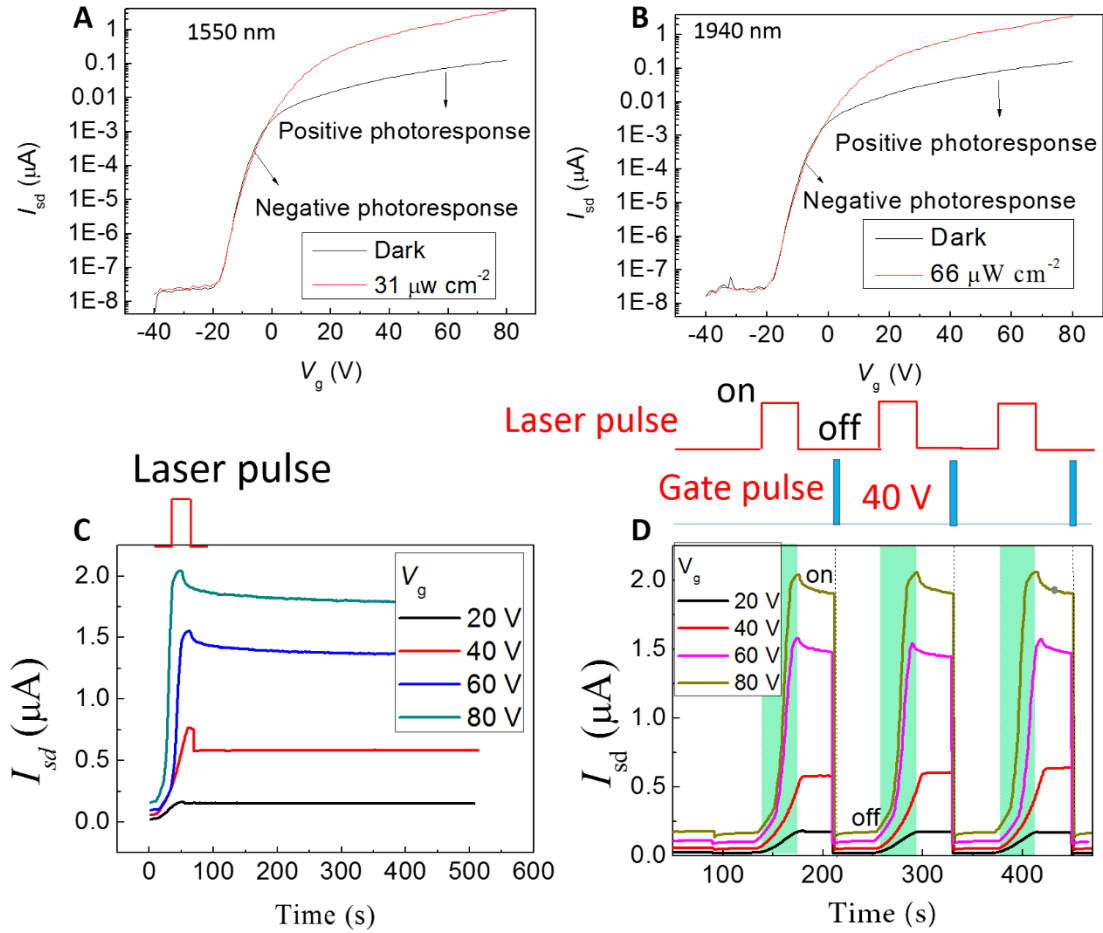**fig. S4**. **Photoresponse in PbS nanoplate with 808 nm laser illumination.**

fig. S5. **The optoelectronic transport and optical memory.** (**A** and **B**) Photoresponse of 1550 and 1940 nm lasers illumination in device #2, respectively. The thickness of few-layer MoS₂ is 6 nm. The channel length L=11.88 μm and width W=7.10 μm. The photocurrent changes from positive to negative with decreasing V_g, which is similar to the case of 808 nm illumination with a low power density in device #1. (**C**) 1940 nm pulse-induced persistent photoconductivity with variable V_g. The laser pulse width is 40 s. The P is 27 μW cm⁻². (**D**) Cycles of laser pulse writing and V_g pulse erasing.
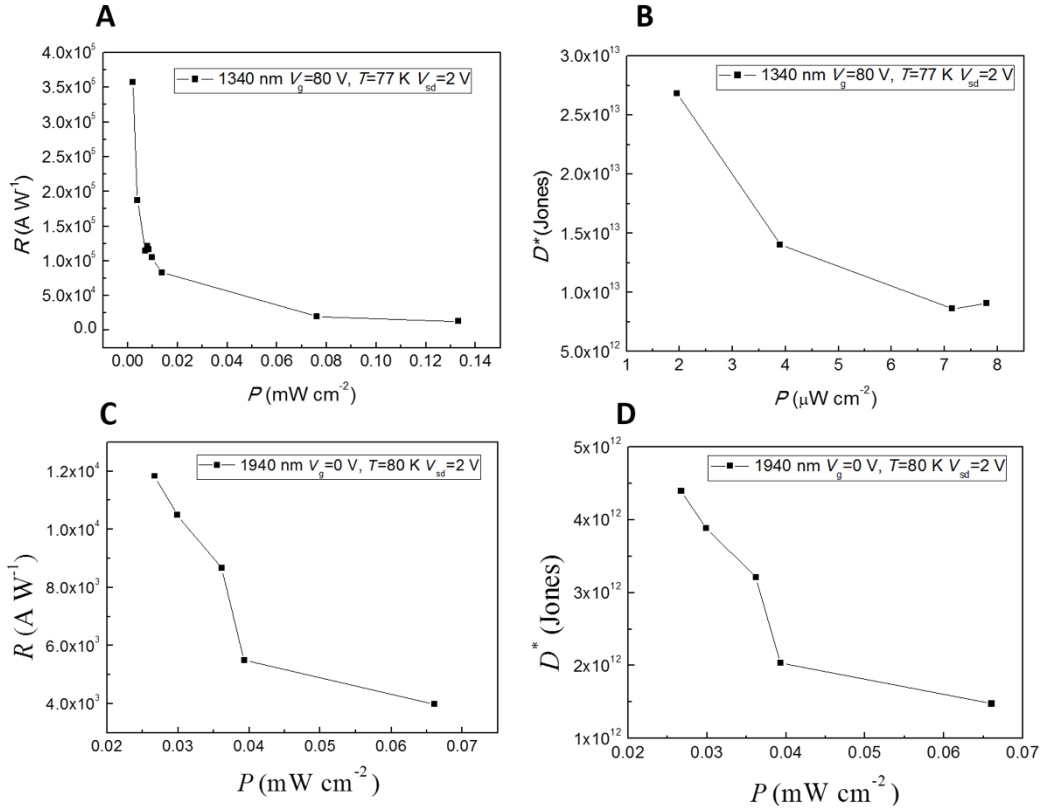
fig. S6. **Photoresponse performance.** (**A** and **B**) The photoresponsivity R and specific detectivity D^* for 1340 nm laser illumination in device #1, respectively. (**C** and **D**) The photoresponsivity R and specific detectivity D^* for 1940 nm laser illumination in device #1, respectively.
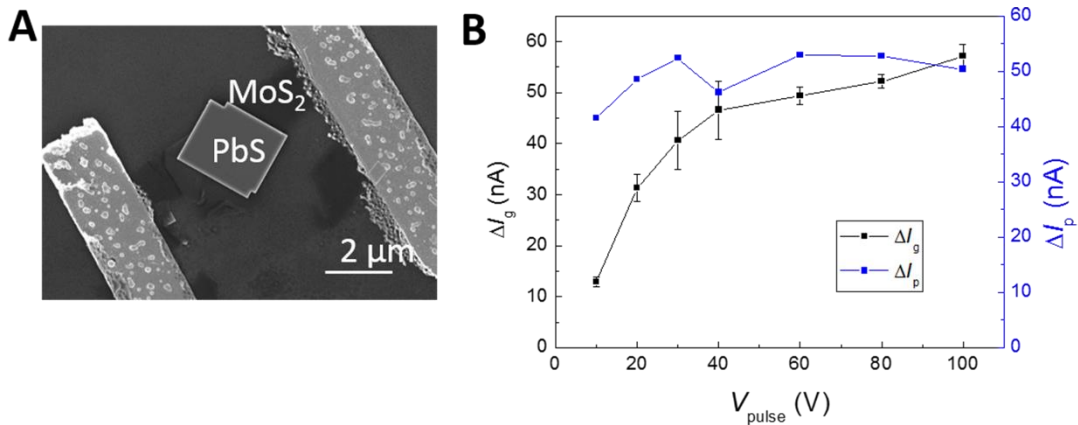
fig. S7. V_g **pulse-dependent erasing current.** (**A**) SEM image of device #3. (**B**) The decrease of I_{sd} (ΔI_g) induced by V_g pulse and photo-generated increase of I_{sd} (ΔI_p) as a function of V_g pulse in device #3. The ΔI_g gradually increases and finally approaches to ΔI_p, while ΔI_p is independent to V_g pulses. The data are extracted from Fig. 5A.
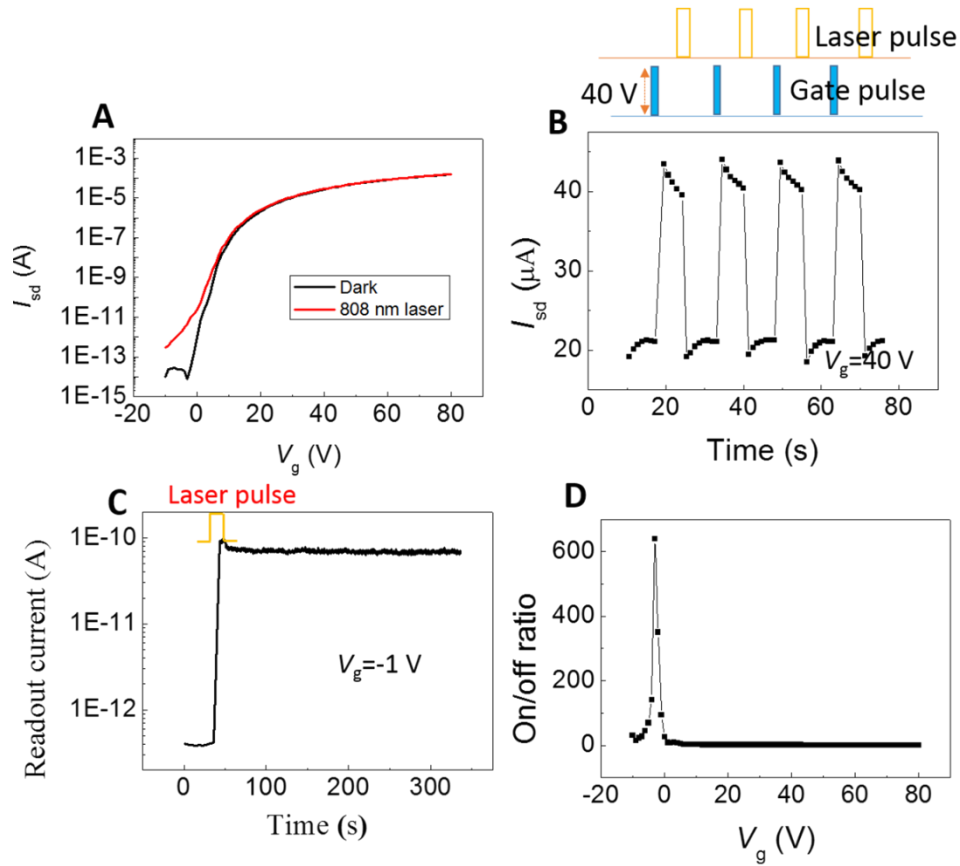
fig. S8. **Optoelectronic transport and on/off ratio.** (**A**) Transfer characteristic curves with 808 laser illumination in device #4. The power density $P = 69.7\ \mu W\ cm^{-2}$. The $V_{sd} = 10$ V. (**B**) The cycles of laser pulse writing and V_g pulse erasing. (**C**) Plot of persistent photocurrent versus time with an on/off ratio of 150. (**D**) V_g dependence of the on/off ratio. With V_g in the depletion region ($V_g = -3$ V), an on/off ratio is ~600 due to the decrease of dark currents. However, if V_g further decreases, the signal intensity also drops, resulting in a reduction of the on/off ratio.

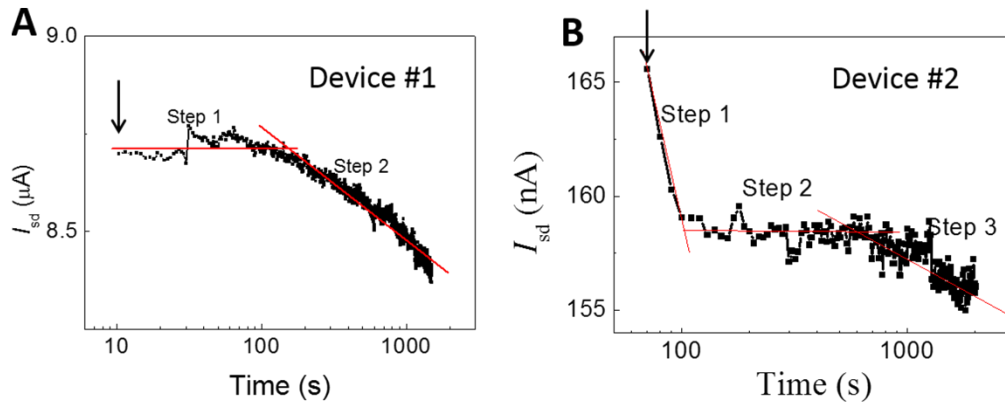**fig. S9**. **Persistent photocurrent as a function of time after the laser pulse switches off.** The black arrow shows when the laser pulse removes. The device #1 (A) shows two decay processes: an almost unchanged process (step 1) and a nearly logarithmic decay process (step 2). The device #2 (B) presents similar decay dynamics as device #1 except an additional logarithmic decay at the beginning.

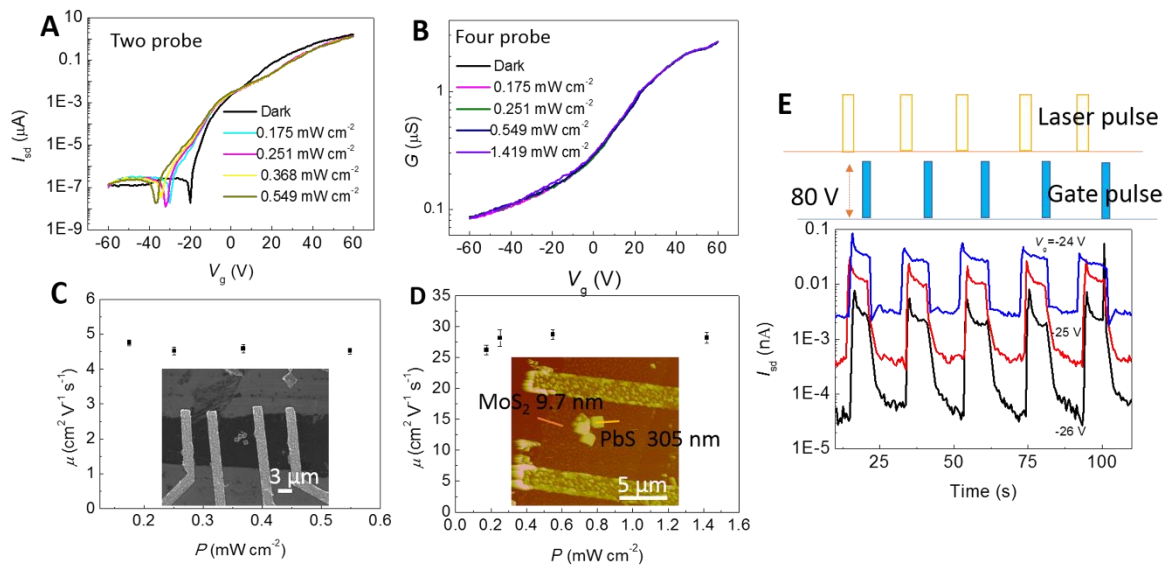**fig. S10. Optoelectronic transport and optical memory.** Transfer characteristic curves by (**A**) two-probe and (**B**) four-probe methods in device #5. Laser power density dependence of the carrier mobility extracted from (**C**) two-probe and (**D**) four-probe measurements. Insets of (C) and (D) are SEM and AFM images of device #5, respectively. (**E**) Cycles of laser pulse writing and V_g pulse erasing.
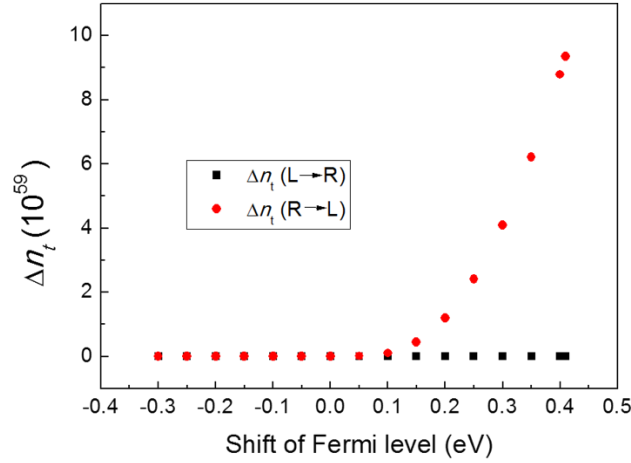
fig. S11. **Number of transferred electrons as a function of the Fermi level shift.** The Δn_t (L→R) and Δn_t (R→L) respectively represents the number of transferred electrons from PbS to MoS_2 and from MoS_2 to PbS after illumination of laser pulses.

table S1. Memory performance of five devices.

	Device #1	Device #2	Device #3	Device #4	Device #5
Operation speed ($\tau_{writing}$ / $\tau_{erasing}$)	15.7 ms / 0.17 s	40.5 s / 1.15 s	1.27 s / 1.45 s	7.64 s / 1.38 s	2.41 s / 2.47 s
Energy consumption (writing / erasing)	420 pJ / 1.50 pJ	910 pJ / 8.00 pJ	2.90 nJ / 0.44 pJ	5.40 nJ / 1.46 pJ	138 pJ / 31.1 pJ
On/off ratio	1.30	16.0	5.00	150	38.0

note S1. Theoretical simulation of carrier injection to MoS₂.

In order to explain our experiment results, we present a physical model based on the transport of thermionic emission and diffusion. For a clear description of our model, we first define several physical parameters as follows: n_e and n_p is the intrinsic electron and hole density in MoS₂ respectively, Δn_{gate} is the change of carriers density due to the back gate field effect (V_g-injection), Δn_{photo} is the change of carriers density in MoS₂ due to carrier injection of photo-excited electrons from PbS (photo-injection), $\Delta n_{e(\text{photo})}$ and $\Delta n_{e(\text{gate})}$ respectively denotes the change of electron density by photo-injection and V_g-injection, and $\Delta n_{p(\text{photo})}$ and $\Delta n_{p(\text{gate})}$ respectively represents the change of hole density by photo-injection and V_g-injection.

We first give the expression of the change of carrier density in MoS₂ due to the carrier injection by photoexcitation and back gate field effect. The device consists of few-layer MoS₂ flakes and PbS nanoplates. The width of the MoS₂ channel is labeled by W, the thickness by T and the length by L. Since infrared radiation is slightly absorbed by MoS₂, photo-generated electrons and holes in MoS₂ should be very small which can be neglected. The charge quantity Q_p generated by photoexcitation is described by $\eta Pte/h\nu$, where e indicates the elementary charge, η is the photoelectric conversion efficiency decided by the absorption coefficient of PbS nanoplates and injection efficiency of infrared-excited electrons from PbS to MoS₂, t represents the duration of infrared illumination, h denotes the Plank constant divided by 2π, and ν is the infrared frequency. Then photo-injection carrier density Δn_{photo} from PbS to MoS₂ is $\Delta n_{\text{photo}} = Q_p/V_{MoS_2} = \eta Pt/V_{MoS_2}e\nu$.

The Δn_{gate} modulated by the gate voltage in MoS₂ can be estimated by

$$\Delta n_{\text{gate}} = \frac{C_g\left(V_g - V_T\right)}{eV_{MoS_2}} \tag{E1}$$

where C_g, V_g, V_T and V_{MoS_2} are the gate capacitance, gate voltage, threshold gate voltage and the volume of MoS₂ nanosheet, respectively. The gate capacitance of our samples can be obtained by $C_i = \varepsilon_0\varepsilon_r/d$ and $C_g = C_iWL$, where d is the thickness of SiO₂ layer, and ε_0 and ε_r

are vacuum dielectric constant and relative dielectric constant of SiO$_2$ layer, respectively. Equation (E1) then evolves into

$$\Delta n_{\text{gate}} = \frac{\varepsilon_0 \varepsilon_r \left(V_{\text{g}} - V_{\text{T}} \right)}{Tde} = \frac{\varepsilon_0 \varepsilon_r \Delta V_{\text{g}}}{Tde} \tag{E2}$$

where $\Delta V_{\text{g}} = V_{\text{g}} - V_{\text{T}}$. Then Δn_{gate} can be separated into two regions based on distribution of ΔV_{g}

$$\Delta n_{\text{gate}} = \begin{cases} \dfrac{\varepsilon_0 \varepsilon_r \Delta V_{\text{g}}}{Tde}, & \Delta V_{\text{g}} > 0 \quad (\text{n-type}) \\[3mm] -\dfrac{\varepsilon_0 \varepsilon_r \Delta V_{\text{g}}}{Tde}, & \Delta V_{\text{g}} < 0 \quad (\text{p–type}) \end{cases} \tag{E3}$$

table S1.1 shows the values of various physical parameters used for calculating laser power density- and V_{g}-modulated Δn of MoS$_2$ shown in Fig. 1E.

table S1.1. Numerical values of various physical parameters.

Parameters	T	d	ε_0	ε_r	η	t	V_{MoS_2}	h	υ
Values	20 nm	280 nm	8.85×10^{-12} F m^{-1}	3.9	3×10^{-3}	1 s	0.25 µm^3	6.6×10^{-34} J s	3.75×10^{14} Hz

We deduce the relation between the current density and carrier density. The current density can be calculated through the thermionic emission theory (*37*). In a dark condition, the current density contributed by electrons J_e is

$$J_e = A_n^* T^2 \exp\left(-\frac{q\phi_{ns}}{k_0 T}\right)\left[\exp\left(\frac{qV_{sd}}{k_0 T}\right) - 1\right] \tag{E4}$$

where A_n^* is the effective electron Richard constant, ϕ_{ns} is the electron barrier height between the Au electrode and MoS$_2$ nanosheet, k_0 denotes the Boltzmann constant, and T is the temperature. V_{sd} is the voltage between source and drain. The current density contributed by holes J_h is given by

$$J_h = A_h^* T^2 \exp(-\frac{q\phi_{ps}}{k_0 T})[\exp(\frac{qV_{sd}}{k_0 T}) - 1] \tag{E5}$$

where A_h^* is the effective hole Richard constant, and ϕ_{ps} is the hole barrier height between the Au electrode and MoS$_2$ nanosheet. The total dark current J_d is

$$J_d = J_e + J_h \tag{E6}$$

The barrier height between the Au electrodes and the MoS$_2$ nanosheet is decided by the quasi Fermi level (37), which is related to the carrier density by

$$n_e = N_c \exp(-\frac{E_c - E_{Fn}}{k_0 T}) \tag{E7}$$

$$n_p = N_v \exp(-\frac{E_{Fp} - E_v}{k_0 T}) \tag{E8}$$

where E_c and E_v are energy levels of the conduction and valance band respectively, E_{Fn} and E_{Fp} are Fermi levels of electrons and holes respectively, and N_c and N_v imply the carrier density of the conduction and valence band respectively. The barrier heights of the energy band in the conduction band and valence band are decided by the carrier densities. Then equations (E7) and (E8) can be evolved into

$$E_c - E_{Fn} = k_0 T \ln(\frac{N_c}{n_e}) \tag{E9}$$

$$E_{Fp} - E_v = k_0 T \ln(\frac{N_v}{n_p}) \tag{E10}$$

First, we consider the case when $\Delta V_g = V_g - V_T > 0$. We get the relationships of carrier densities and band energy as

$$n_e + \Delta n_{e(\text{photo})} + \Delta n_{e(\text{gate})} = N_c \exp(-\frac{E_c - E'_{Fn}}{k_0 T}) \tag{E11}$$

$$n_p - \Delta n_{p(\text{photo})} + \Delta n_{p(\text{gate})} = N_v \exp(-\frac{E'_{Fp} - E_v}{k_0 T}) \tag{E12}$$

where E'_{Fn} and E'_{Fp} are respectively the Fermi levels of electrons and holes after photo-injection and V_g-injection. We ignore the change of hole density by the gate field effect ($\Delta n_{p(\text{gate})}$) and photo-injection ($\Delta n_{p(\text{photo})}$) since they are much smaller than the change of electron density. These two equations can be evolved to

$$n_e + \Delta n_{e(\text{photo})} + \Delta n_{e(\text{gate})} = N_c \exp(-\frac{E_c - E'_{Fn}}{k_0 T}) \tag{E13}$$

$$n_p = N_v \exp(-\frac{E'_{Fp} - E_v}{k_0 T}) \tag{E14}$$

Then, we get

$$E_c - E'_{Fn} = k_0 T \ln(\frac{N_c}{n + \Delta n_{e(\text{photo})} + \Delta n_{e(\text{gate})}}) \tag{E15}$$

$$E'_{Fp} - E_v = k_0 T \ln(\frac{N_v}{n_p}) \tag{E16}$$

Combining with the intrinsic relationship

$$E_c - E_{Fn} = k_0 T \ln(\frac{N_c}{n_e}) \tag{E17}$$

$$E_{Fp} - E_v = k_0 T \ln(\frac{N_v}{n_p}) \tag{E18}$$

the variations of electron and hole barrier height after the photo-injection and V_g-injection are

$$\Delta \phi_{ns} = (E'_{Fn} - E_{Fn})/q = \frac{k_0 T}{q} \ln(\frac{n_e + \Delta n_{e(\text{photo})} + \Delta n_{e(\text{gate})}}{n_e}) \tag{E19}$$

$$\Delta\phi_{ps} = (E_{Fn} - E_{Fp}^{'})/q = \frac{k_0 T}{q}[\ln(\frac{N_v}{n_p}) - \ln(\frac{N_v}{n_p})] = 0 \qquad (E20)$$

The current density $J_e^{'}$ contributed by photo-injection and V_g-injection is

$$J_e^{'} = A_n^* T^2 \exp(-\frac{q\phi_{ns} + q\Delta\phi_{ns}}{k_0 T})[\exp(\frac{qV}{k_0 T}) - 1] = \frac{n_e}{n_e + \Delta n_{e(photo)} + \Delta n_{e(gate)}} J_e \qquad (E21)$$

The current density contributed by photo-generated holes $J_h^{'}$ is

$$J_h^{'} = A_h^* T^2 \exp(-\frac{q\phi_{ps} - q\Delta\phi_{ps}}{k_0 T})[\exp(\frac{qV}{k_0 T}) - 1] = J_h \exp(\frac{q\Delta\phi_{ps}}{k_0 T}) = J_h \qquad (E22)$$

The total current density with illumination and gate voltage is

$$J_{total} = J_{photo} + J_{gate} + J_{dark} = J_e^{'} + J_h^{'} = \frac{n_e}{n_e + \Delta n_{e(gate)} + \Delta n_{e(photo)}} J_e + J_h \qquad (E23)$$

In this work, we define the moving direction of electrons as the direction of current. Then the change of the current density ΔJ is

$$\Delta J = J_{total} - J_d = \frac{\Delta n_{e(gate)} + \Delta n_{e(photo)}}{n_e + \Delta n_{e(gate)} + \Delta n_{e(photo)}} J_e \qquad (E24)$$

Then, we consider the case when $\Delta V_g = V_g - V_T < 0$. Similarly, we get

$$n_e + \Delta n_{e(photo)} = N_c \exp(-\frac{E_c - E_{Fn}^{'}}{k_0 T}) \qquad (E25)$$

$$n_p + \Delta n_{p(gate)} = N_v \exp(-\frac{E_{Fp}^{'} - E_v}{k_0 T}) \qquad (E26)$$

The barrier height variations of electrons and holes are respectively

$$\Delta\phi_{ns} = (E'_{Fn} - E_{Fn})/q = \frac{k_0 T}{q} \ln(\frac{n_e + \Delta n_{e(\text{photo})}}{n_e}) \qquad (E27)$$

$$\Delta\phi_{ps} = (E_{Fn} - E'_{Fp})/q = \frac{k_0 T}{q} \ln(\frac{n_p + \Delta n_{p(\text{gate})}}{n_p}) \qquad (E28)$$

The current density J'_e and J'_h contributed by photo-generated and gate-injected carries are

$$J'_e = A_n^* T^2 \exp(-\frac{q\phi_{ns} + q\Delta\phi_{ns}}{k_0 T})[\exp(\frac{qV}{k_0 T}) - 1] = \frac{n_e}{n_e + \Delta n_{e(\text{photo})}} J_e \qquad (E29)$$

$$J'_h = A_h^* T^2 \exp(-\frac{q\phi_{ps} - q\Delta\phi_{ps}}{k_0 T})[\exp(\frac{qV}{k_0 T}) - 1] = \frac{n_p + \Delta n_{p(\text{gate})}}{n_p} J_h \qquad (E30)$$

The total current density with illumination and gate voltage is

$$J_{total} = J_{photo} + J_{gate} + J_{dark} = J'_e + J'_h = \frac{n_e}{n_e + \Delta n_{e(\text{photo})}} J_e + \frac{n_p + \Delta n_{p(\text{gate})}}{n_p} J_h \qquad (E31)$$

The change of the current density ΔJ related to the change of carrier density is given by

$$\Delta J = J_{\text{total}} - J_d = \frac{\Delta n_{e(\text{photo})}}{n_e + \Delta n_{e(\text{photo})}} J_e - \frac{\Delta n_{p(\text{gate})}}{n_p} J_h \qquad (E32)$$

The equation (E32) explains the positive-to-negative transition of photocurrents as V_g shifts to around or below 0 V at various P as shown in Fig. 1D. The first term $\Delta n_{e(\text{photo})} J_e/(n_e + \Delta n_{e(\text{photo})})$ on the right side expresses the current density contributed by photo-injected electrons and shows a positive value. However, the second term $-\Delta n_{e(\text{gate})} J_h/n_p$ comes from V_g-injected holes, and becomes more and more negative with decreasing V_g. In the case of $\Delta V_g < 0$, V_g drops to the region where the holes are accumulated and electrons are depleted. However, when $\Delta V_g > 0$, ΔJ is always positive since electrons from photo-injection and V_g-injection dominate the current (see equation (E24)).

note S2. Dynamics analysis of V_g pulse erasing.

Figure 4A shows the band diagram of the few-layer MoS$_2$-PbS heterostructure after photo-injection. A depletion and an accumulation layer respectively forms on the left (PbS) and right (MoS$_2$) side. A barrier forms due to misalignment of energy bands between two materials. A typical energy barrier is $\Delta E = E_{cr} - E_{cl}$, where E_{cl} and E_{cr} are the bottom of the conduction bands of PbS and MoS$_2$, respectively. Photo-excited holes are bounded in PbS nanoplates. In notes 1, we have discussed the electron injection into MoS$_2$ with two independent factors of the back gate voltage and illumination.

After photo-injection at time $t = t_1$ (Fig. 3C), the charge flows across the junction barrier of MoS$_2$-PbS heterostructure via two mechanisms of thermionic emission and quantum tunneling. First, we consider the charge transfer by tunneling. The transmission probability through the barrier is given by

$$T_t \approx A(E)\exp\left\{-2\int_{x_1}^{x_2}\sqrt{\frac{2m^*}{\hbar^2}\Delta E(x)}dx\right\} \tag{E33}$$

where $A(E)$ is a smooth function that is dependent on the details of wave-function matching at the interface. $\Delta E(x) = U(x) - E$, E is energy of the barrier, $U(x)$ is the energy of electron depending on the position of the conduction band. For simplify, we assume $A(E)$ as a constant in our model. The tunneling current density $J_{L\to R}^T$ from PbS (left) to MoS$_2$ (right) (Fig. 4A) can be expressed as

$$J_{L\to R}^T = \frac{qm^*}{2\pi^2\hbar^3}\int_{E_{cl}}^{E_{cl}+\Delta E} F_L(E)N_L T_t(E)\left(1 - F_R(E)\right)N_R dE \tag{E34}$$

where $F_L(E)$ and $F_R(E)$ are the Fermi distribution function of PbS and MoS$_2$ respectively.

The current density $J_{L\to R}^E$ via thermionic emission of electrons with the energy higher than the barrier is

$$J_{L\to R}^E = \frac{qm^*}{2\pi^2\hbar^3}\int_{E_{cl}+\Delta E}^{+\infty} F_L(E)N_L\left(1 - F_R(E)\right)N_R dE \tag{E35}$$

The total current density from left to right is

$$J_{L \to R} = J_{L \to R}^{T} + J_{L \to R}^{E} \tag{E36}$$

Similarly, the tunneling and thermionic emission current density from the right to left can be respectively expressed as

$$J_{R \to L}^{T} = \frac{qm^{*}}{2\pi^{2}\hbar^{3}} \int_{E_{cr}}^{E_{cl}+\Delta E} F_{R}(E) N_{R} T_{t}(E)(1 - F_{L}(E)) N_{L} dE \tag{E37}$$

and

$$J_{R \to L}^{E} = \frac{qm^{*}}{2\pi^{2}\hbar^{3}} \int_{E_{cl}+\Delta E}^{+\infty} F_{R}(E) N_{R} (1 - F_{L}(E)) N_{L} dE \tag{E38}$$

The total current density from right to left is

$$J_{R \to L} = J_{R \to L}^{T} + J_{R \to L}^{E} \tag{E39}$$

The net current density across the junction is

$$J_{total} = J_{L \to R} - J_{R \to L} \tag{E40}$$

Then, the net current should be

$$I_{total} = J_{total} S \tag{E41}$$

In MoS$_2$, the carrier density is given by

$$n_{e} = N_{c} \exp(-\frac{E_{c} - E_{F}}{kT}) \tag{E42}$$

By applying a gate voltage V_{g}, it changes into

$$n_e' = n_e + \Delta n = N_c \exp\left(-\frac{E_c - E_F'}{kT}\right) \tag{E43}$$

The shift of the Fermi level is related to Δn by

$$\Delta E_F = E_F' - E_F = kT \ln\left(\frac{n_e + \Delta n}{n_e}\right) = kT \ln\left(1 + \frac{\Delta n}{n_e}\right) \tag{E44}$$

and in the linear region

$$\Delta n = \frac{C_g\left(V_g - V_T\right)}{eV_{MoS_2}} = \alpha \Delta V_g \tag{E45}$$

Then, ΔE_F is related to ΔV_g by

$$\Delta E_F = kT \ln\left(1 + \frac{\alpha \Delta V_g}{n_e}\right) \tag{E46}$$

The gate voltage causes the shift of E_F, which leads to a new equilibrium state. At a given gate voltage pulse with $t = 100$ ms, the current is $I(t)$, and we can get the number of transferred electrons (Δn_t) via $Q = I(t)\Delta t$ as shown in Fig. 4B, where Q is the charge quantity.

note S3. Roles of disorder states on the optical memory.

The transition metal dichalcogenides normally contain chalcogen vacancies acting as the efficient electron traps (*38*). As mentioned above the MoS_2 device is unresponsive to 1940 nm laser pulses (fig. S3C). While 1940 nm laser pulses can intrigue the optical memory in the MoS_2-PbS heterostructure (fig. S5). In addition, PbS nanoplates did not present any observable persistent photocurrent (fig. S4). Therefore, the optical memory effect is the intrinsic effect of MoS_2-PbS heterostructure rather than impurities or defects. We then analyze the decay process of laser induced photocurrents in the logarithmic time scale (fig. S9). We find localized defects or impurities states such as S vacancies possibly affect the writing speed of laser pulses (*39*). However, they are not the dominant factor to form the persistent photoconductivity. With removing of the laser pulse, the photocurrent relaxes through the recombination of photo-excited electrons with holes. As proposed by Theodorou *et al.* (*27*), the logarithmic decay is the indication of spatial separation of carriers. Wide junction regions or trap-free buffer layers create the charge-free region which leads to a non-decay persistent photocurrent within $t = \tau_0 \left[\exp(2w/a) - 1 \right]$ and then a logarithmic decay, where τ_0 is the lifetime for eliminating the charge spatial separation, w is width of charge-free region and a is the Bohr radius. As shown in fig. S9A, the photocurrent undergoes two decay processes in device #1. At the beginning ($10 < t < 112$ s, step 1), there is essentially no obvious decay after removing the laser pulse. Then the photocurrent shows a near logarithmic decay (step 2). This decay phenomenon strongly indicates that the optical memory effect in our devices is due to the space separation of photo-excited electrons and holes. The holes are trapped in PbS while the electrons are injected into the MoS_2 transport channel (Fig. 1B). This eventually results in a charge-free region which prevents the trapped holes from recombination by electrons in the MoS_2 layer. The disorder states in the heterostructure indeed affect the decay process of persistent photocurrents in some devices. As shown in fig. S9B (device #2), the photocurrent initially follows a logarithmic decay (step 1), suggesting the disorder states possibly trap the photo-injected electrons and slowly release after removing the laser pulse (*25*). We note that device #2 also displays a slow writing speed (fig. S5D). This likely originates from disorders states trapping the photo-injected electrons. However, after the decay process of step 1, the photocurrent in step 2 and step 3 presents the similar decay behavior as device #1. We then conclude that the dominant optical memory mechanism in our devices is due to the potential barrier separating the photo-excited electrons and holes rather than random localized potential fluctuations from defects or

impurities. Based on this mechanism, we can further improve the charge storage stability by increasing the width of charge-free region. The buffer layer at the interface likely enhances the charge storage duration (27).

note S4. Photothermal effect or Schottky barrier effect.
The PbS nanoplates are possible local heat sources due to the photothermal effect. However, this cannot be the physical origin of optical memory. For the photothermoelectric effect, the middle PbS nanoplates cannot establish the temperature difference between two electrodes in the MoS$_2$ transport channel. Taking device #5 as an example, the PbS nanoplates are uniformly distributing in the middle of MoS$_2$ layer (fig. S10). Considering the lifetime (~50 ps) of hot carriers (40) in MoS$_2$ and carrier mobility (~27 cm^2 V^{-1} s^{-1}) in device #5, the transport length of hot carriers is ~34.3 nm which is far less than the distance from PbS nanoplates to the electrodes (~2.0-2.5 μm). The short diffusion length (~10 nm) of hot carriers in MoS$_2$ has been also confirmed by a previous work (41), which means hot carriers completely decay before reaching electrodes, giving rise to zero photothermoelectric voltage ($V_{PTE} = S\Delta T$), where S is the Seebeck coefficient and ΔT is the temperature difference between two electrodes. Since the lifetime of excited states for both phonons (picoseconds) (42) and carriers (nanoseconds) (40) in MoS$_2$ is too short to sustain the persistent photocurrent, the bolometric effect cannot be the dominant mechanism to contribute photocurrents.

The nonlinear I_{sd}-V_{sd} curves in fig. S2C indicates the non-Ohmic contact in our devices. This arises from the Schottky barriers forming at the interface of MoS$_2$ and metal electrodes. However, the few-layer MoS$_2$ layer (fig. S3) shows no observable persistent photocurrent, which excludes the Schottky barrier as an origin of the optical memory. The Schottky barrier affects the estimation of the carrier mobility by two-probe methods, which has been well studied previously (43). The four-probe measurement could rule out the contribution from contacts. As shown by fig. S10, the four-probe method gives rise to a higher mobility than that from the two-probe method. However, four-probe and two-probe method present a similar trend that the carrier mobility slightly changes with the laser power intensity P within our measurement range.